RSC Advances

PAPER

View Article Online
View Journal | View Issue

Cite this: *RSC Adv.*, 2025, **15**, 25221

Optimizing hybrid supercapacitor performance through synergistic integration of metal–organic frameworks and metal oxides

Waqas Shoukat, *[a] M. Z. Iqbal,[b] Imran Murtaza, *[a] Prakash Kanjariya, [c] Asha Rajiv,[d] Debasish Shit,[e] Helen Merina Albert,[f] Satish Kumar Samal,[g] Abhinav Kumar[hij] and Saikh M. Wabaidur*[k]

Metal–organic frameworks (MOFs) offer significant advantages for energy storage, including high surface area, customizable porosity, and abundant active sites. We utilized these properties to synthesize a novel barium-MOF and neodymium oxide composite (Ba-MOF/Nd_2O_3) as an electrode material for hybrid supercapacitors. Incorporating Nd_2O_3—a lanthanide-series rare-earth metal oxide—enhances the composite's electrochemical properties, particularly in terms of specific capacity, energy density, power density, and cyclic stability. In a half-cell setup, the composite provided a remarkable specific capacity of 718 C g^{-1} at the lowest current density (1.9 A g^{-1}). For further investigation, a real device was functionalized, which provided better energy density of 96 Wh kg^{-1} with a maximum power density of 9350 W kg^{-1}. The device exhibited a rate capability of 96% and capacity retention of 92%, even after the 5000 charge–discharge process. Furthermore, semi-empirical models were employed to assess the capacitive and diffusive contributions.

Received 7th February 2025
Accepted 20th June 2025

DOI: 10.1039/d5ra00911a

rsc.li/rsc-advances

1. Introduction

In the developing world, the growing use of electrical appliances has led to an increasing demand for electrical energy.[1] Non-renewable resources are inadequate to meet this demand owing to depletion and ecological concerns.[2,3] Renewable energy resources exhibit unstable availability and inconsistency. Consequently, they require intermediate storage solutions for consistent power supply.[4,5] In the realm of electrochemical energy storage devices (EESDs), supercapacitors (SCs) and rechargeable batteries (RBs) are leading trends owing to their superior electrochemical performance and potential to mitigate the energy crisis.[6–8] Batteries excel in energy density and specific capacity, but several factors, such as low power, lower lifespan, and safety hazards, hamper their practical applications. Conversely, although SCs are known for their high power density, durability, and environmental friendliness, their low energy density constrains their application.[9,10] Consequently, each technology alone cannot fully meet the commercial requirements. To address these challenges, engineers have developed hybrid energy storage devices that combine the strengths of supercapacitors and rechargeable batteries known as hybrid supercapacitors (HSCs).[11–13]

An effective strategy to boost the performance of HSCs is to endow an electrode material with superior electrochemical properties.[2,14] Various electrode materials have been explored to enhance the electrochemical performance of HSCs, including conducting polymers,[15,16] carbon-based material,[17–20] layered hydroxide,[21,22] transition metal oxides,[23,24] phosphates,[25,26] sulfides[27–29] and selenides.[30] Despite these materials, metal–organic frameworks (MOFs) have attracted significant attention as energy storage systems due to their exceptional structural and functional attributes.[31–33] The metal–ligand structure provides a remarkably high surface area, crucial for maximizing

[a]*Flexible Electronics Laboratory (FEL), Department of Physics, International Islamic University, Islamabad, 44000, Pakistan. E-mail: waqas.phdphy116@iiu.edu.pk; imran.murtaza@iiu.edu.pk*

[b]*Faculty of Engineering Sciences, Ghulam Ishaq Khan Institute of Engineering Sciences and Technology, Topi, 23640, Khyber Pakhtunkhwa, Pakistan*

[c]*Marwadi University Research Center, Department of Physics, Faculty of Science, Marwadi University, Rajkot-360003, Gujarat, India*

[d]*Department of Physics & Electronics, School of Sciences, JAIN (Deemed to be University), Bangalore, Karnataka, India*

[e]*Centre for Research Impact & Outcome, Chitkara University Institute of Engineering and Technology, Chitkara University, Rajpura, 140401, Punjab, India*

[f]*Department of Physics, Sathyabama Institute of Science and Technology, Chennai, Tamil Nadu, India*

[g]*Department of Electronics & Communication Engineering, Siksha 'O' Anusandhan (Deemed to be University), Bhubaneswar, Odisha-751030, India*

[h]*Department of Nuclear and Renewable Energy, Ural Federal University Named after the First President of Russia Boris Yeltsin, Ekaterinburg 620002, Russia*

[i]*Advanced Research and Development Center, LIPS Research Foundation, European International University, Paris, France*

[j]*Department of Mechanical Engineering and Renewable Energy, Technical Engineering College, The Islamic University, Najaf, Iraq*

[k]*Department of Chemistry, College of Science, King Saud University, Riyadh, 11451, Saudi Arabia. E-mail: swabaidur@ksu.edu.sa*

active sites involved in electrochemical reactions.[34] The high surface area and adjustable porosity enable efficient electrolyte transport and enhanced charge storage capacity. The tunable porosity of MOFs allows for customization of their properties to meet specific energy storage requirements.[35] Despite these advantages, some pristine MOFs are often limited by poor electrical conductivity and instability, which can affect their efficiency in energy storage solutions.[36,37]

Alkaline earth metals (AEMs) such as radium, strontium, and barium are important for creating MOFs due to their divalent nature and large ionic size, which support the development of stable architectures.[38] In particular, barium shows great promise in energy storage applications. Its larger ionic radius enables a highly adaptable coordination environment, which allows the creation of diverse and stable structural frameworks with enhanced porosity and surface area. Besides, carboxylate ligands are excellent at coordinating with metal ions through their oxygen atoms, providing multiple binding sites that enable the formation of large and stable networks.[39] These ligands are suitable for building MOFs because they establish strong connections with metal ions.[40] Despite their remarkable properties, pristine MOFs face several limitations that hinder their performance in energy storage systems. They typically exhibit low electrical conductivity, limited ion diffusion, and reduced mechanical strength, which can lead to poor long-term capacity retention.[36]

Besides, metal oxides—particularly those from the rare-earth lanthanide series—offer several advantages for energy storage applications. Their high reactivity, large surface-to-volume ratio, and catalytic properties contribute to improved charge storage capacity and energy density. However, their application can be constrained by high costs and limited availability. Furthermore, metal oxides can suffer from reduced durability in energy storage applications owing to their highly reactive nature. Hybridizing MOFs with functional materials such as metal oxides to create composites mitigates the shortcomings of parent materials.[41,42]

Herein, the synthesis of Ba-MOF was carried out through hydrothermal treatment, followed by the fabrication of a composite incorporating commercially available neodymium oxide (Nd_2O_3). Subsequently, the composite was employed as an electrode material to strengthen the electrochemical response of the hybrid supercapacitor. The incorporation of Nd_2O_3 not only enhances the structural stability of the composite but also improves its electrochemical performance. The composite demonstrated superior performance, attaining a specific capacity (Q_s) of 718 C g^{-1} (C_s of 1026 F g^{-1}) at 1.9 A g^{-1}. To assess the practical applicability of the composite, an HSC device was assembled, delivering the energy density (E_d) of 96 Wh kg^{-1} with a power density (P_d) of 765 W kg^{-1} at a current density of 0.9 A g^{-1}. Furthermore, the device achieved the highest P_d of 9350 W kg^{-1} while preserving the E_d of 26 Wh kg^{-1} at 11 A g^{-1}. For examination of capacitive and diffusive contributions in full-cell assembly, theoretical models (*i.e.*, linear and quadratic models) were compared. The findings suggest that Ba-MOF/Nd_2O_3 holds significant potential as an electrode for future energy storage technology.

2. Experimental procedure

2.1. Materials

All available solvents, metal salts, binders, electrolytes, and metal salts were utilized without additional refinement. The reagents included barium chloride ($BaCl_2$), trimesic acid, nickel foam, *N*-methyl-2-pyrrolidone (NMP), polyvinylidene fluoride (PVDF), acetylene black, and potassium hydroxide (KOH), all obtained from Urich Technology. The other chemicals were sourced from Sigma-Aldrich, including hydrochloric acid (HCl, 37%) and dimethyl formamide (DMF).

2.2. Synthesis of Ba-MOF

To synthesize Ba-MOF, 0.5 M of $BaCl_2$ was first dissolved in 20 mL of deionized water and ultrasonicated for 30 min. Simultaneously, 0.3 M of trimesic acid was poured into another beaker with 15 mL of deionized water and stirred for 30 min. For the uniform dispersion of trimesic acid, 5 mL of DMF was also added. Then, the solutions were gradually combined while stirring. After the complete dissolution and uniformity, the precursor solution was placed in an autoclave and calcined at 180 °C for 24 h. The product was obtained through centrifugation and thoroughly rinsed with methanol and deionized water. Ultimately, the material was dried at 70 °C overnight in a furnace.[43,44]

2.3. Synthesis of Ba-MOF/Nd_2O_3

Ba-MOF/Nd_2O_3 was synthesized by dissolving 0.5 M of commercially sourced Nd_2O_3 in 20 mL of deionized (DI) water, followed by stirring on a magnetic stirrer. In a separate beaker, 0.3 M $BaCl_2$ was dissolved in 15 mL of DI water and stirred. Concurrently, 0.2 M trimesic acid was added to a mixture of 15 mL of DI water and DMF and stirred for 30 minutes to ensure complete dissolution. Once prepared, the $BaCl_2$ solution was slowly introduced into trimesic acid solution while stirring to achieve thorough mixing. Subsequently, the Nd_2O_3 solution was gradually added to the combined mixture, ensuring homogenous dispersion. Following this, the prepared solution was introduced into an autoclave and annealed at 180 °C for 24 h. Subsequent steps followed the same protocol described for Ba-MOF synthesis. The experimental work is portrayed in Fig. 1.

2.4. Electrode fabrication

For electrode preparation, nickel foam (NF) with dimensions of (1 × 1.5 cm^2) were used as the substrate to assess the electrochemical performance of the synthesized materials. Ten mL slurries were prepared for each electrode, containing 80 wt% of active materials, 10 wt% of acetylene black, and 5 wt% of both PVDF and NMP. Subsequently, the slurries were stirred for 6 hours to prepare a homogeneous solution. Then, the prepared solutions were deposited onto NF, covering it half-length (1 × 0.75 cm^2) by utilizing a micropipette. Finally, the electrodes were dried in a furnace at 70 °C for 4 h.[45]

To assess the real device, a cathodic electrode (AC) was fabricated with PVDF, AC, NMP, and acetylene black using the

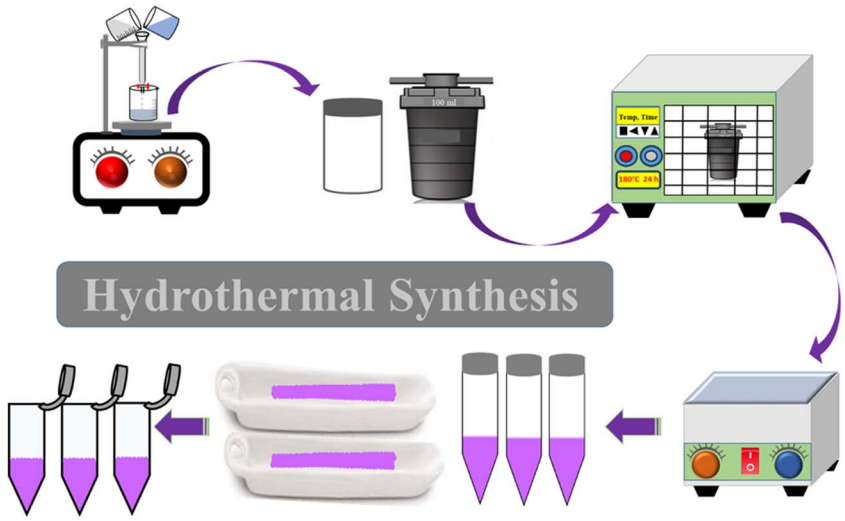

Fig. 1 Schematic illustrating the synthesis of electrode materials.

previously described method. The mass balance was calculated using the equation given below:[46]

$$\frac{m_+}{m_-} = \frac{C_{s_-} \times \Delta V_-}{C_{s_+} \times \Delta V_+} \quad (1)$$

Here m_+ and C_+ are the mass loading and capacitance of the anodic electrode, respectively, while m_- and C_- denote the mass loading and capacitance of the cathodic electrode, respectively.

3. Results and discussion

3.1. Physicochemical characterization

X-ray diffraction (XRD) was conducted to examine the structural order and phase composition of the fabricated materials. Fig. 2(a) shows the XRD pattern of Ba-MOF, revealing its cubic crystalline structure with well-defined peaks indexed according to (JCPDS 96-900-8529).[47] The sharpness and high intensity of the peaks suggest good crystallinity and phase purity of the material. Similarly, the XRD pattern of Nd_2O_3 exhibits distinct peaks indexed according to (JCPDS 00-043-1023),[48] revealing its hexagonal crystalline structure, as portrayed in Fig. 2(b). Fig. 2(c) presents the XRD pattern of Ba-MOF/Nd_2O_3 with well-defined peaks corresponding to both Ba-MOF and Nd_2O_3, confirming the coexistence of the two phases within the composite material. The small shift in some XRD peaks of the composite is likely due to lattice strain, partial diffusions, or partial diffusion of Nd^{3+} ions into the Ba-MOF structures. Additionally, internal stress, defects, or changes in crystallite size could contribute to this shift.[49] The peak's sharpness and consistency reveal good crystallinity, suggesting that both components retained their structural integrity during composite formation.

Fig. 2(d–h) provides the intricate spatial distribution of the elements present within the material, especially Ba, C, O, and Nd. The observed slight inhomogeneity in elemental

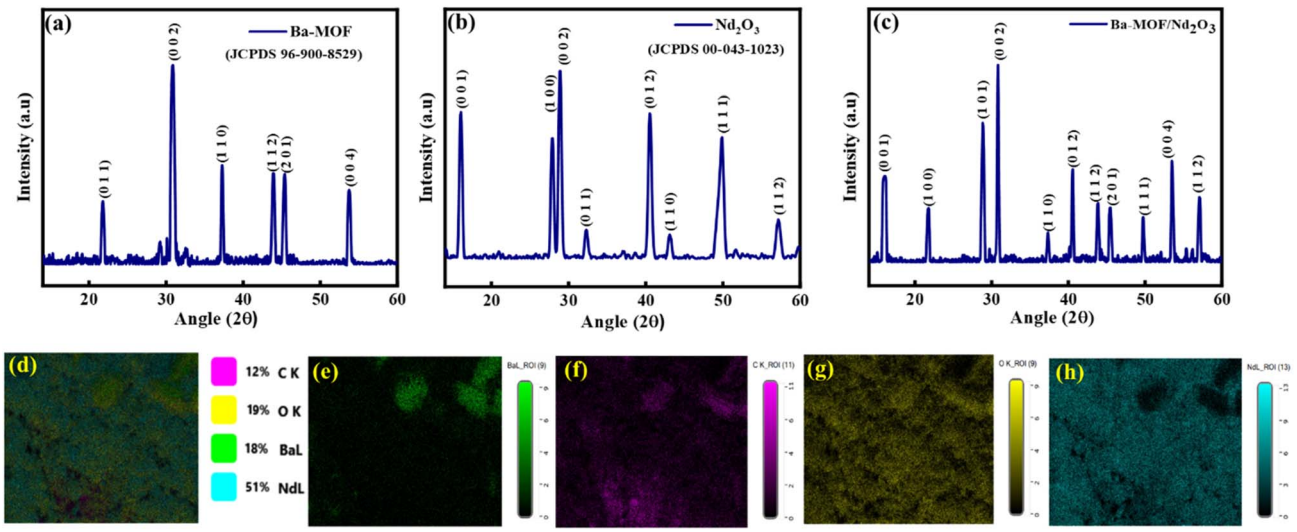

Fig. 2 (a) XRD patterns of Ba-MOF (b) Nd_2O_3 (c) Ba-MOF/Nd_2O_3 composite. (d–h) Elemental mapping of the Ba-MOF/Nd_2O_3 composite.

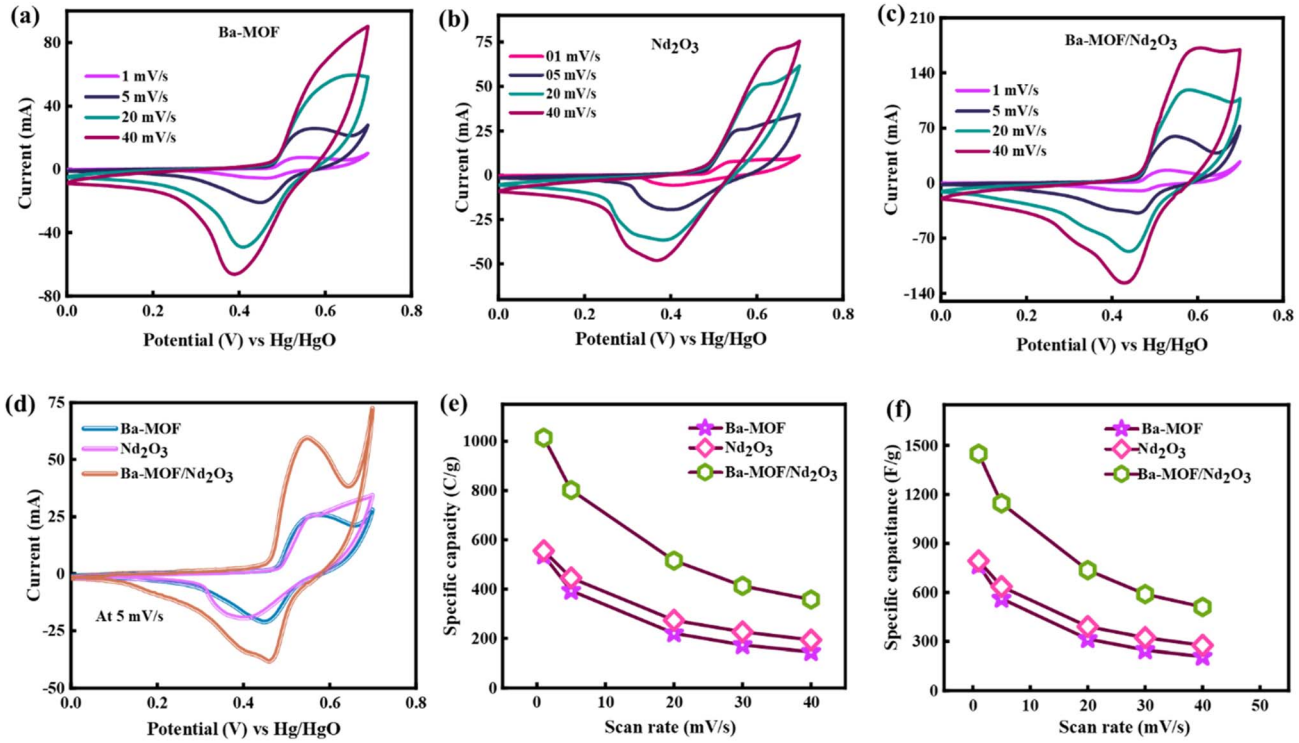

Fig. 3 Cyclic curves of (a) Ba-MOF (b) Nd_2O_3 (c) Ba-MOF/Nd_2O_3 at various scan rates. (d) Comparative CV at 5 mV s^{-1}. (e) Q_s of fabricated electrodes through CV at various scan rates. (f) C_s of fabricated electrodes through CV at various scan rates.

distribution may be attributed to surface roughness and local agglomeration of Nd_2O_3 within the Ba-MOF framework; however, the presence of all key elements confirms successful composite formation. Better homogeneity is achieved during the slurry preparation process for electrochemical testing, where uniform mixing ensures consistent electrode performance.

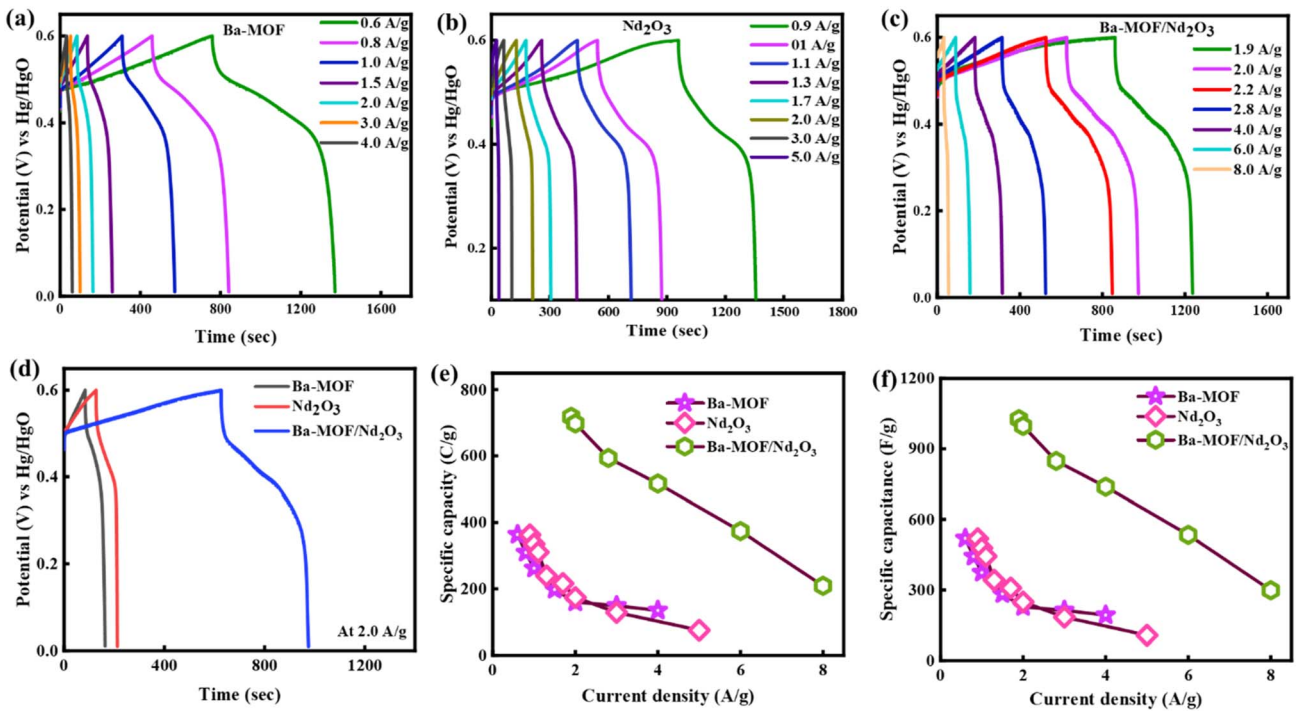

Fig. 4 GCD cycles at various current densities (a) Ba-MOF (b) Nd_2O_3 (c) Ba-MOF/Nd_2O_3. (d) Comparative GCD at 1.9 A g^{-1} (e). Q_s of fabricated electrodes at various current densities. (f) C_s of fabricated electrodes at various current densities.

3.2. Electrochemical characterization

3.2.1 Half-cell measurements. The electrochemical performance of Ba-MOF, Nd_2O_3, and Ba-MOF/Nd_2O_3 was initially assessed in a half-cell setup with 1 M potassium hydroxide as the electrolyte. Cyclic voltammetry (CV) analysis was executed at various scan rates (1–40 mV s^{-1}) between 0-0.7 V. Fig. 3(a–c) shows that the CV profile of the fabricated electrodes manifested distinct redox peaks characteristic of battery-grade behavior and stable faradaic reactions within the electrode materials.[50]

Notably, the Ba-MOF/Nd_2O_3 composite exhibited higher current values and a larger area under the CV profile compared with Ba-MOF and Nd_2O_3, underscoring its enhanced electrochemical performance, as shown in the comparative graph (Fig. 3(d)). The variation in redox peak positions in the CV profile of electrodes arises from alteration of the electrode composition and interaction between Ba-MOF and Nd_2O_3. Incorporation of Nd_2O_3 into the MOF matrix introduces new redox-capable centers and alters the electronic configuration surrounding the Ba sites. Moreover, the reduction peaks in the composite CV curves show prominent humps, which can be attributed to surface heterogeneity and the presence of multiple redox-active sites from both Ba-MOF and Nd_2O_3. These humps reflect the complex redox interactions and synergistic effect within the composite, where multiple redox processes occur at different potentials, enhancing its capacity. Additionally, the expanded CV of the composite at higher scans highlights its increased charge storage ability and enhanced electrochemical characteristics. Specific capacity was computed by employing the relation given below.[51]

$$Q_s = \frac{\int I \times dV}{m \times \nu} \quad (2)$$

Here, Q_s denotes specific capacity (C g^{-1}), the integral term represents the area of the CV profile, m refers to the mass load, and ν stands for the scan rate. The Q_s of pristine Ba-MOF and Nd_2O_3 is relatively lower, whereas their composite feedback is significantly enhanced. Pristine Ba-MOF and Nd_2O_{33} exhibited specific capacities of 536 C g^{-1} and 555 C g^{-1}, correspondingly, while the Ba-MOF/Nd_2O_3 composite achieved a much higher specific capacity of 1014 C g^{-1} at the lowest scanning rate. This improvement results from a strong synergistic effect between Ba-MOF and Nd_2O_3 in the composite structure. Nd_2O_3 is a rare-earth metal oxide that possesses a high oxygen vacancy concentration and good redox reversibility, which can contribute to pseudocapacitive behavior. These oxygen vacancies facilitate faster ion diffusion and may enhance surface faradaic reactions during the charge–discharge process. However, when used alone, Nd_2O_3 exhibits limited electrochemical performance owing to poor conductivity and a low surface area. In the composite form, Ba-MOF provides a porous and conductive framework that accommodates Nd_2O_3 particles, while Nd_2O_3 improves the electrochemical reactivity and conductivity of the MOF structure. This complementary interaction improves charge transfer kinetics and structural integrity. Therefore, the Ba-MOF/Nd_2O_3 composite benefits from both components, with the porous nature of Ba-MOF enhancing ion transport and redox-active Nd_2O_3 contributing to higher pseudocapacitance. This enhanced performance of the composite highlights its potential for superior energy storage applications. The value of Q_s and C_s of all the electrodes at different sweep rates is depicted in Fig. 3(e and f).

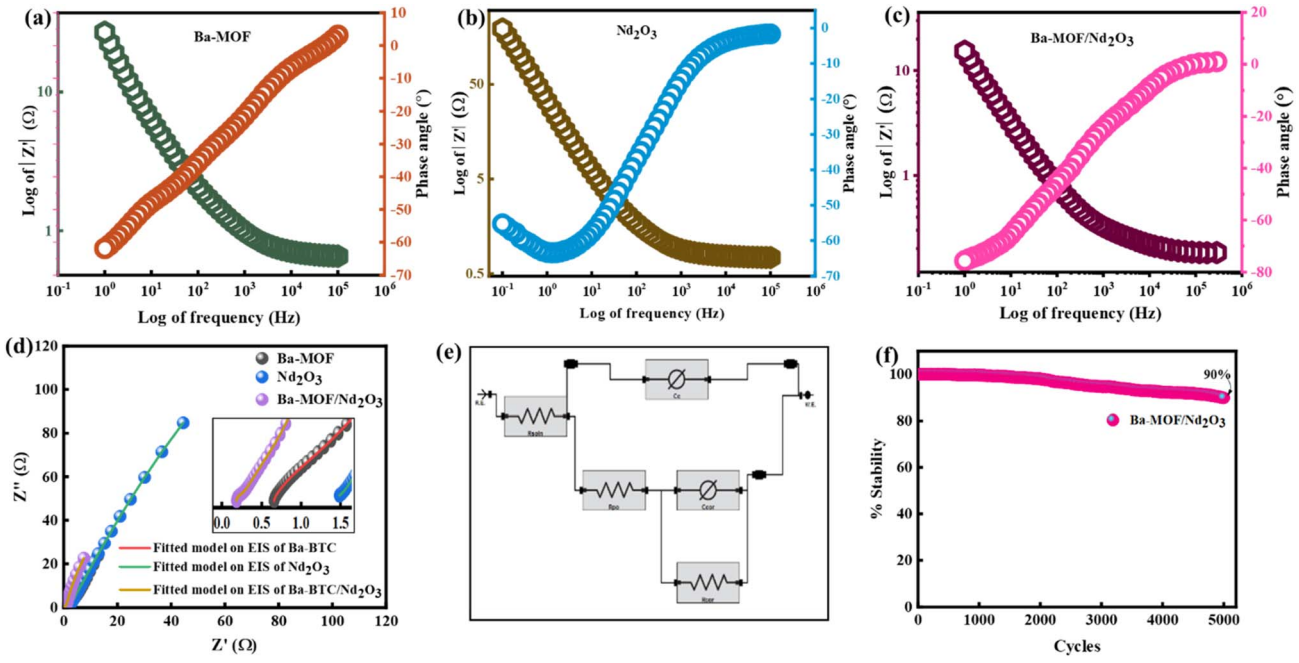

Fig. 5 (a) Bode plot of Ba-MOF. (b) Bode plot of Nd_2O_3. (c) Bode plot of Ba-MOF/Nd_2O_3. (d) Nyquist plot of fabricated electrodes with its zoomed part in the inset. (e) Fitted model circuit. (f) Cyclic stability of the composite.

Thereafter, GCD testing was conducted at a potential of 0.6 V across various current densities. The non-linear behavior in the discharging profile further reinforces the battery-grade characteristics of synthesized product, consistent with the confirmation from CV analysis, as portrayed in Fig. 4(a–c). Fig. 4(d) illustrates the comparative analysis of various electrodes at 2 A g^{-1}. The prolonged discharge duration of the Ba-MOF/Nd_2O_3 composite in comparison with Ba-MOF and Nd_2O_3 alone highlights the enhanced energy storage capability of the composite, in agreement with the earlier CV analysis. The high-rate capability is highlighted by symmetrical responses under higher scans and current density. Additionally, the Q_s values were determined from GCD analysis by applying the subsequent expression:[52]

$$Q_s = \frac{I \times \Delta t}{m} \quad (3)$$

Here, I stands for current, Δt refers to the discharge profile, and m corresponds to mass loading of the fabricated material.

The Ba-MOF and Nd_2O_3 achieved Q_s values of 363 C g^{-1} and 362 C g^{-1} at 0.6 A g^{-1} and 0.9 A g^{-1}, respectively, reflecting the inherent electrochemical behavior of each material. In contrast, the Ba-MOF/Nd_2O_3 composite exhibited a significantly enhanced Q_s of 718 C g^{-1} at 1.9 A g^{-1}, highlighting the superior performance of the composite. This enhancement in the specific capacity is primarily due to synergistic effects between the Ba-MOF and Nd_2O_3, which combine the individual advantages of both materials. These synergistic effects result in an increased number of active sites for redox reactions, enhanced electron conductivity, and more efficient ion diffusion within the composite structure.

Additionally, the composite's improved structural integrity contributes to better cyclic stability, reducing material degradation over time and enabling more effective charge storage. The enhanced conductivity minimizes internal resistance, leading to faster electron transport and more efficient energy transfer during charge–discharge cycles. Besides, the porous structure of the composite likely provides a larger surface area

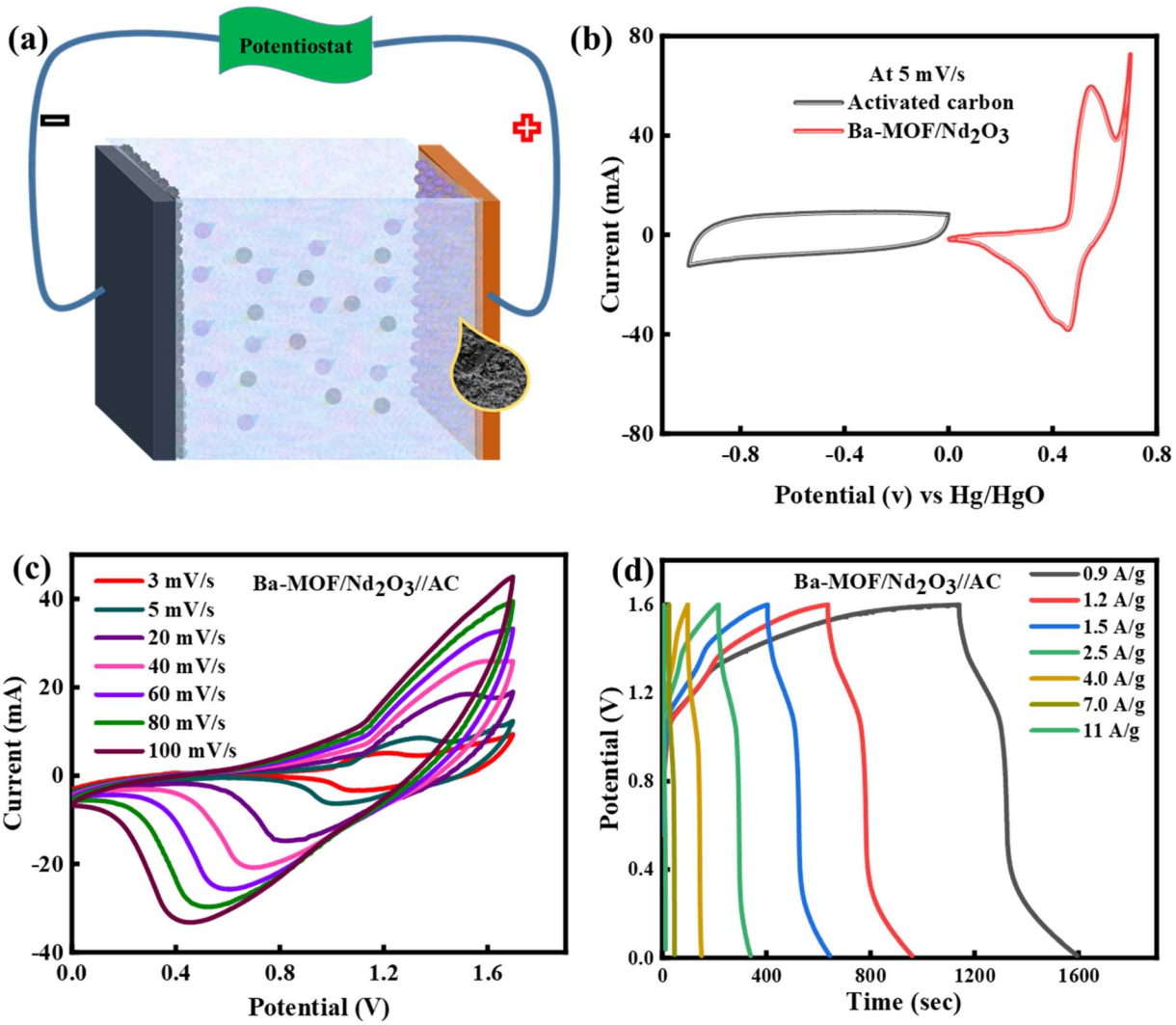

Fig. 6 (a) Schematic of the device. (b) CV curve of both battery grade and capacitive electrodes at 5 mV s^{-1} (c) CV graph of the assembled device (Ba-MOF/Nd_2O_3//AC). (d) GCD investigation of the device.

and better electrolyte penetration, promoting faster ion diffusion and more uniform charge distribution. These combined factors contribute to the composite's significantly higher specific capacity compared with the individual materials, making it a more effective electrode for energy storage applications. The calculated Q_s and C_s values from GCD analysis are demonstrated in Fig. 4(e and f).

To investigate the conductive behavior and associated parameters of the fabricated electrode materials, EIS measurements were carried out over a frequency range of 0.1–100 kHz with an applied voltage of 10 mV. Fig. 5(a–c) is the Bode plot for Ba-MOF, Nd_2O_3, and their composite, where the log of impedance magnitude and phase angle are plotted against the log of frequency. The double *y*-axis plot reveals the frequency-dependent behavior of both impedance and phase shift. The composite material delivered the lowest impedance at a lower frequency range, demonstrating the best performance compared with Ba-MOF and Nd_2O_3, offering superior electrochemical performance. This lower impedance suggests that the synergy between Ba-MOF and Nd_2O_3 optimizes ion transport and reduces energy losses more effectively than either individual component. At the intermediate frequency region, the slope of the magnitude of the impedance decreases, reflecting an increase in resistive dominance. At higher frequencies, the impedance magnitude levels off and becomes nearly parallel to the *x*-axis, indicating pure resistive behavior, corresponding to the equivalent series resistance (ESR), which will be further discussed in the Nyquist plot. Similarly, the composite shows the maximum value of the phase angle in the Bode plot (near −90°), indicating more capacitive dominant behavior compared with an individual, and is beneficial for energy storage applications. Fig. 5(d) is the Nyquist plot with the fitted model, which demonstrates significant improvement in the conductivity of the Ba-MOF after the incorporation of Nd_2O_3. The inset of Fig. 5(d) particularly emphasizes this enhancement at high frequencies. The Ba-MOF/Nd_2O_3 exhibited the smallest equivalent series resistance (ESR = 0.35 Ω) compared with the individual samples owing to improved electron transport and enhanced ion diffusion. The combination of two materials creates more efficient pathways for both ions and electrons, reducing internal resistance. Additionally, the optimized interface between Ba-MOF and Nd_2O_3 minimizes charge transfer resistance, contributing to the lower ESR value. The Nyquist plot displays no noticeable semicircle, suggesting a low interfacial resistance to charge transfer at the electrode surface. A shorter linear segment in the composite points to decreased

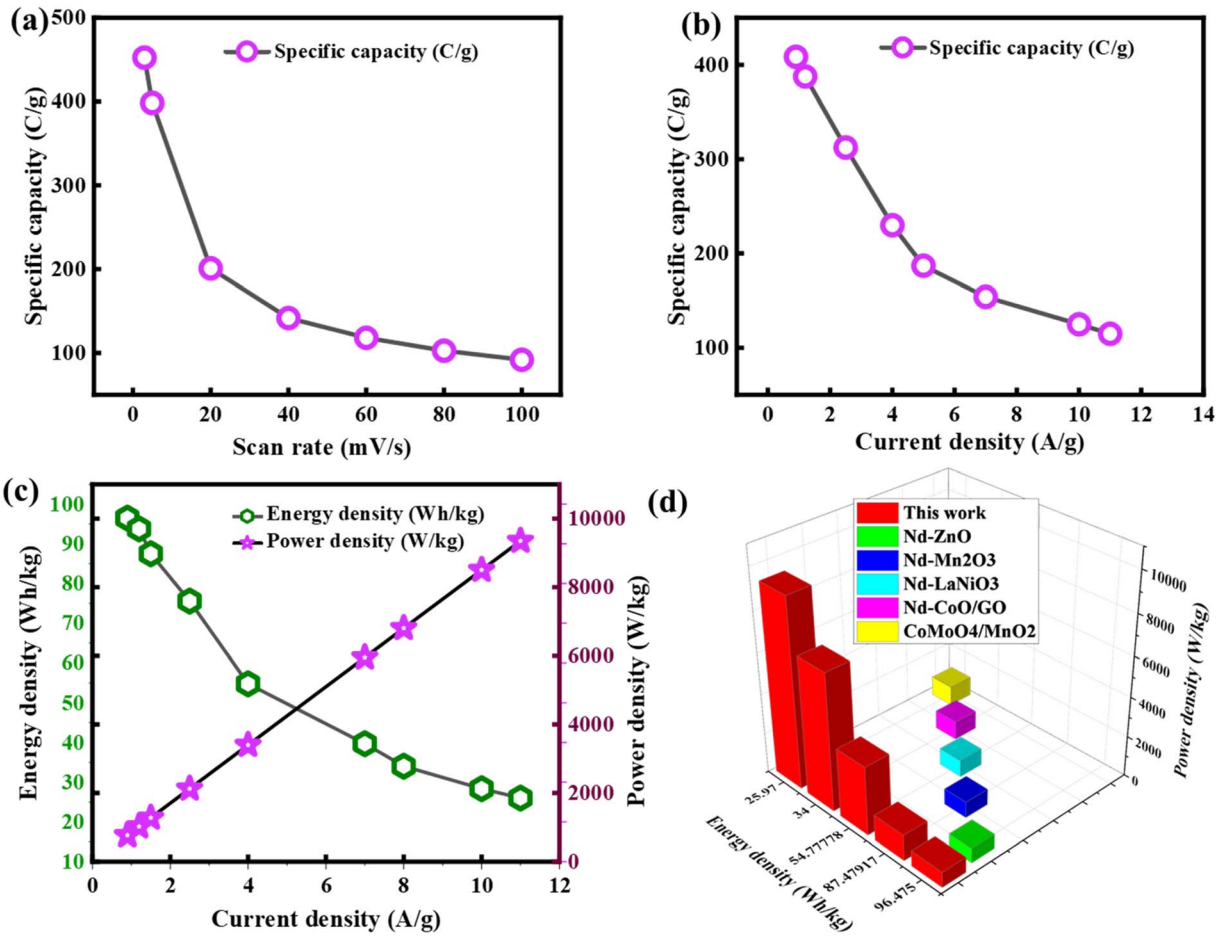

Fig. 7 (a) Q_s of the assembled device at various scan rates. (b) Q_s of the assembled device at various current densities. (c) Energy *vs.* power plot of the device. (d) Comparison with previous literature.

Warburg resistance (W_b) compared with Ba-MOF and Nd_2O_3 alone, reflecting improved ion transport. This improved ion transport likely results from an interconnected structure in the composite, which enhances charge transfer and supports faster charge/discharge rates, boosting its overall electrochemical performance. Fig. 5(e) shows the circuit of the fitted model on the EIS data points of Ba-MOF, Nd_2O_3, and Ba-MOF/Nd_2O_3. Additionally, cyclic stability was tested over 5000 cycles, and the composite retained 90% of its initial capacity, as presented in Fig. 5(f). The results from CV, GCD, and EIS analysis highlight the exceptional electrochemical performance of Ba-MOF/Nd_2O_3, positioning it as a suitable contender for future hybrid energy storage technology.

3.2.2 Full-cell measurements. The capability of the synthesized material was further examined by using the best-performing electrode (Ba-MOF/Nd_2O_3) as an anodic electrode, along with AC in 1 M KOH. The cyclic voltammetric study was conducted across a 3–100 mV s^{-1} scan rate, with a potential of 0–1.7 V. The schematic complete-cell setup and individual CV profile of Ba-MOF/Nd_2O_3 and AC at 5 mV s^{-1} are depicted in Fig. 6(a and b). The CV curves of the cell shown in Fig. 6(c) demonstrate a hybrid-shape profile, indicating a combination of battery-like and capacitive behavior. This hybrid shape reflects the synergistic combination of the faradaic redox reaction at the Ba-MOF/Nd_2O_3 electrode and the double-layered capacitance behavior of the AC electrode. The symmetric response at high scan rates underscores its excellent rate capability and electrochemical stability.

Additionally, GCD assessment was performed at 1.6 V potential over a broad regime of current densities (0.9–11 A g^{-1}) to evaluate its charge–discharge characteristics, as depicted in Fig. 6(d). The GCD profiles show linear segments typical of capacitive behavior, while the minor inflections in the discharge portion point to the participation of battery-like redox reactions. The device demonstrated an impressive Q_s of 452 C g^{-1} and 408 C g^{-1} at the lowest scan rate and current density, respectively. Fig. 7(a and b) demonstrated the variation of Q_s with various scan rates and current densities. Key electrochemical performance metrics namely, energy density and power density are calculated with the following relations.[53]

$$E_d = \frac{Q_s \times \Delta V}{2 \times 3.6} \quad (4)$$

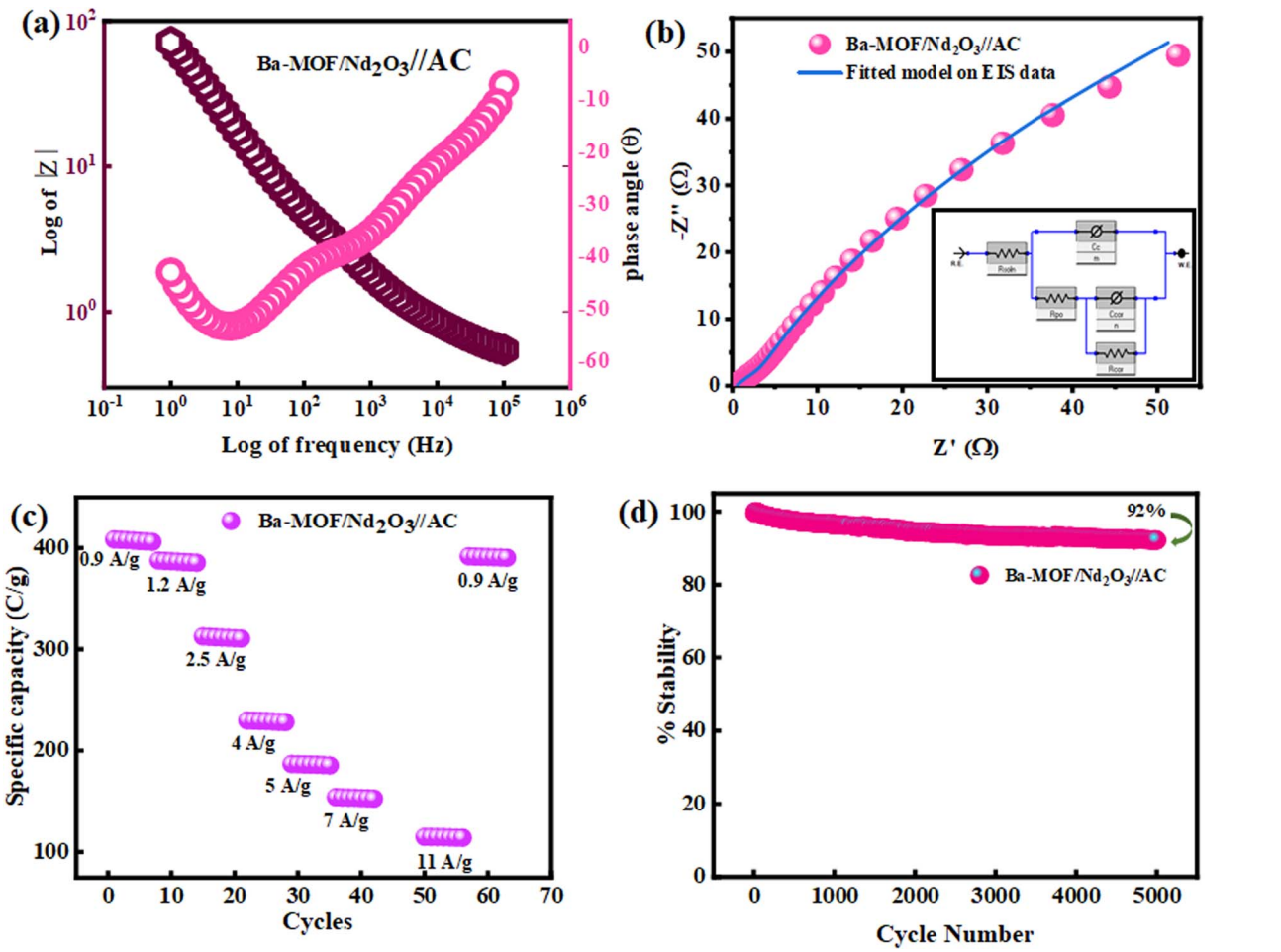

Fig. 8 (a) Bode plot of the device. (b) Nyquist plot of the device. (c) Rate capability of the device. (d) Cyclic stability of the device.

$$P_d = \frac{3600 \times E_s}{\Delta t} \quad (5)$$

In the aforementioned relations, ΔV is the potential window, while Δt represents the discharge time. The device attained an impressive E_d of 96 Wh kg^{-1} and a P_d of 765 Wh kg^{-1} at 0.9 A g^{-1}. Furthermore, the device accomplished an exceptional maximum P_d of 9350 W kg^{-1} while sustaining the E_d of 25.9 Wh kg^{-1} at 11 A g^{-1}. The dependence of energy and power densities on applied current densities is shown in Fig. 7(c), while Fig. 7(d) displays the Ragone plot comparing the fabricated cell to the reported work.[54–58] This evaluation underscores the superior performance of our fabricated device, establishing it as a suitable contender for advanced HSCs.

To assess conductivity and the associated parameters, EIS measurements were performed within a frequency window of 0.1 to 100 kHz at an applied voltage of 10 mV. The Bode plot for Ba-MOF/Nd_2O_3//AC shows a small value of impedance at the low-frequency regime (Fig. 8(a)). The intermediate frequency range shows contributions from both resistive and capacitive behavior, while the response transitions to a purely resistive behavior at higher frequencies. Fig. 8(b) presents the Nyquist plot with its fitted model, revealing a small ESR (0.52 Ω), with an insignificant value of R_{ct}. The low ESR highlights the better intrinsic conductivity of the device, ensuring efficient electron/ion flow with minimal resistance. The negligible R_{ct} reflects highly effective transfer at the electrode–electrolyte interface. Furthermore, the rate capability of the device was evaluated, demonstrating 96% retention, as presented in Fig. 8(c). However, a decrease in capacity is observed with increasing current densities, which is common in battery-grade materials owing to limited ion diffusion time. The device exhibits excellent rate reversibility when the current density is returned to its original value. In addition, stability testing across 5000 consecutive cycles revealed an impressive retention rate of 92%, as illustrated in Fig. 8(d). The slight decline in capacity retention (8% over 5000 cycles) may be attributed to structural distortion in the material, which could lead to a gradual loss of electrochemical activity. Prolonged electrolyte exposure may also contribute to the partial dissolution of active species, particularly from the Ba-MOF phase, thereby compromising long-term stability. Moreover, repetitive charge–discharge cycling could induce interfacial degradation at the active

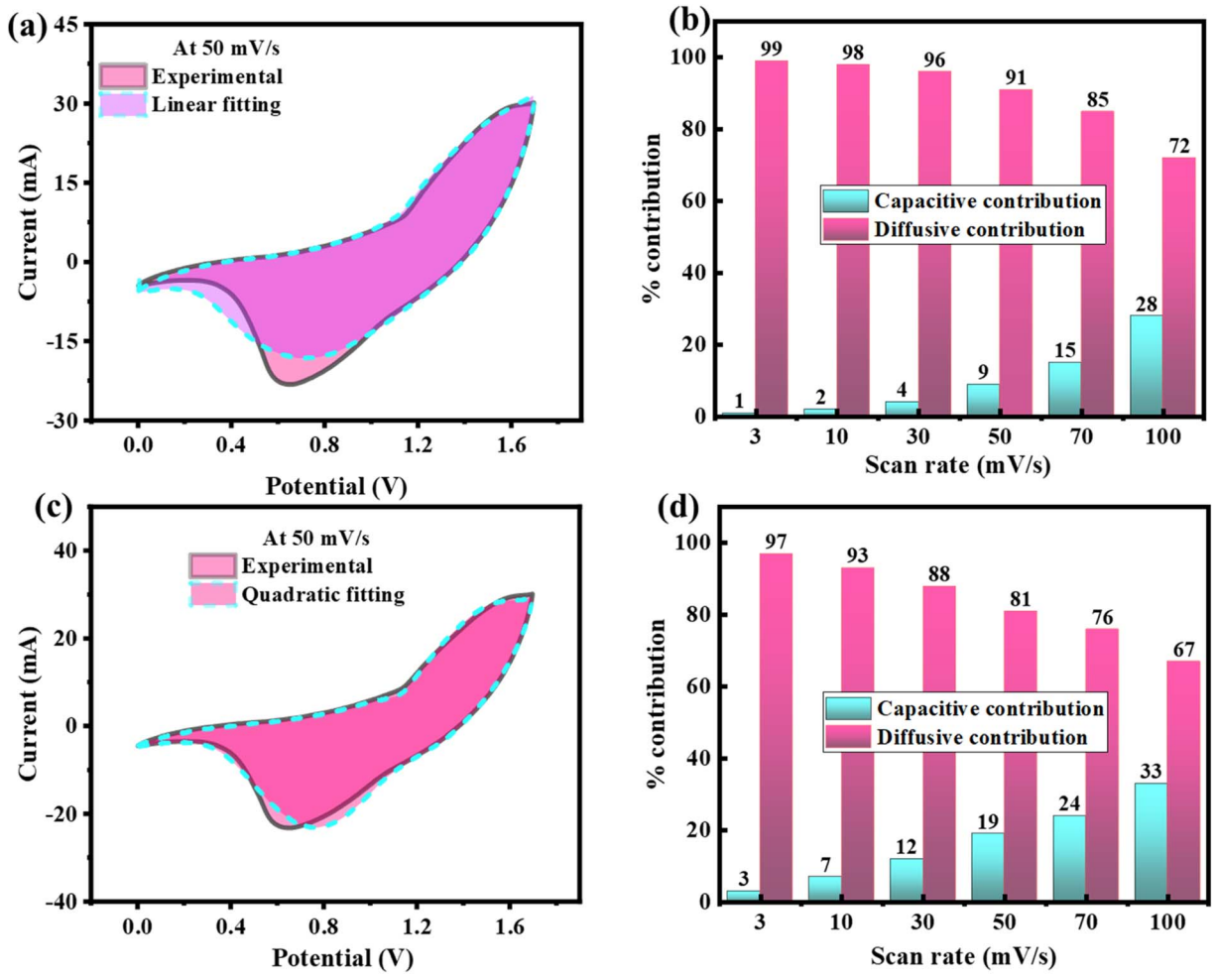

Fig. 9 (a) Linear model fitting of experimental data. (b) Bar graph of capacitive and diffusive contributions by the linear model. (c) Quadratic model fitting of experimental data. (d) Bar graph of capacitive and diffusive contributions by the quadratic model.

material–current collector boundary, resulting in incremental increases in internal resistance. These outcomes highlight the continuous and stable electrochemical performance of the device.

3.3. Semi-empirical analysis

To analyze the capacitive and diffusion-controlled charge storage pathway of the device, two semi-empirical approaches were utilized: linear and quadratic models. The models were utilized on the same device, but the quadratic one proved to be more accurate, closely aligning with the observed behavior.

The total current is determined as a sum of two components: $I_{NF} = k_1 v$ is attributed to non-faradaic current, while $I_F = k_2 v^{1/2}$ demonstrates faradaic current. These currents are determined by employing the following relation.[59]

$$I(v,V) = k_1 v + k_2 v^{1/2} \quad (6)$$

In this equation, v corresponds to the scan rate, while k_1 and k_2 represent the regression parameters. The term $k_1 v$ refers to capacitive contributions, while $k_2 v^{1/2}$ represents the process governed by ion diffusion. Fig. 9(a) demonstrates the linear fitting of the experimental data for the capacitive and diffusive contributions at 50 mV s^{-1}. Although the linear model is effective in capturing basic trends, it struggles when analyzing larger data segments or regions near peaks. Fig. 9(b) showcases the substantial performance of the electrode through a linear model bar graph. The plot highlights the extent to which capacitive and diffusion-driven behaviors influence the charge storage process under varying scan conditions.

To overcome the shortcomings of the linear model, a diffusive correction was integrated. It resulted in a quadratic model, providing a more precise representation of the underlying phenomenon.[60]

$$I(v,V) = \beta_1 v + \beta_2 v^{1/2} + \beta_3 v^{3/2} \quad (7)$$

In the above equation, $\beta_i\,(i = 1, 2, 3)$ are regression parameters, $\beta_1 v$ captures the combined effects of capacitive and pseudocapacitive behavior, whereas $\beta_2 v^{1/2}$ and $\beta_3 v^{3/2}$ account for the diffusive behavior. The quadratic fit depicted in Fig. 9(c) exhibits a significantly improved correlation with the experimental data, highlighting its effectiveness in capturing the observed results. Fig. 9(d) showcases the substantial performance of the electrode through a bar graph. The graph effectively illustrates the respective roles of surface-controlled and ion-diffusion mechanisms in charge retention under various scan rates. The bar graph of linear and quadratic models reveals a progressive decline in diffusive contribution as the scan rate increases. This phenomenon is likely due to the limited time available to complete the redox reaction.

4. Conclusion

In this study, we successfully synthesized Ba-MOF/Nd_2O_3 composite by the hydrothermal approach. Characterization techniques such as XRD, SEM, and EDX were employed to investigate the crystalline structure, morphological features, and elemental distribution of the fabricated material. The electrochemical performance was assessed, showing that Ba-MOF, Nd_2O_3, and their composite achieved 363 C g^{-1}, 362 C g^{-1}, and 718 C g^{-1}, respectively, at the lowest current density. Based on the elevated capability of the composite, a hybrid device was assembled using Ba-MOF/Nd_2O_3 as an anodic electrode and AC as a cathodic electrode. The cell demonstrated a Q_s of 408 C g^{-1} at the lowest current density, with and E_d of 96 Wh kg^{-1} and P_d of 9350 W kg^{-1}. Moreover, it presented impressive cyclic stability by maintaining 92% of its initial capacity even after 5000 consecutive iterations. To further understand the device's behavior, two distinct semi-empirical models were utilized and their results were evaluated against the experimental findings. The comprehensive electrochemical characteristics presented in this study highlight the potential of Ba-MOF/Nd_2O_3 as a favorable electrode material for future hybrid supercapacitor applications. In future work, the electrochemical performance of the Ba-MOF/Nd_2O_3 composite could be further enhanced through strategies such as interfacial engineering, or the introduction of conductive networks to improve charge transport and stability.

Data availability

All the data are provided in the article.

Conflicts of interest

The authors declare that there are no conflicts of interest.

Acknowledgements

The authors would like to extend their sincere appreciation to the Ongoing Research Funding program, (ORF-2025-448), King Saud University, Riyadh, Saudi Arabia. The authors gratefully acknowledge the Ghulam Ishaq Khan Institute of Engineering Sciences and Technology for providing the characterization facilities for this research.

References

1 M. J. E. Khalid, A review on the selected applications of battery-supercapacitor hybrid energy storage systems for microgrids, *Energies*, 2019, **12**(23), 4559.
2 R. Xu, et al., Highly Energy Release of Aluminum@Ammonium Perchlorate Composites Incorporated with Graphene Oxide-based Energetic Coordination Polymer, *Adv. Funct. Mater.*, 2025, **35**(24), 2423205.
3 C. Zhiqiang, *et al.*, Rationally Designed PPy-Coated Fe2O3 Nanoneedles Anchored on NC Nanoflakes as a High-Performance Anode for Aqueous Supercapacitors, *Crystals*, 2025, **15**(4), 346.
4 W. Zuo, *et al.*, Battery-supercapacitor hybrid devices: recent progress and future prospects, *Adv. Sci.*, 2017, **4**(7), 1600539.

5 M. Z. Iqbal and U. J. Aziz, Supercapattery: Merging of battery-supercapacitor electrodes for hybrid energy storage devices, *J. Energy Storage*, 2022, **46**, 103823.
6 F. Zhang, *et al.*, A high-performance supercapacitor-battery hybrid energy storage device based on graphene-enhanced electrode materials with ultrahigh energy density, *Energy Environ. Sci.*, 2013, **6**(5), 1623–1632.
7 H. Hao, *et al.*, Innovating high-performance aqueous sodium-ion batteries with ice-resistant inorganic electrolytes for-40 °C applications, *Energy Storage Mater.*, 2025, **76**, 104149.
8 H. Xu, *et al.*, Lattice Water Deprotonation Enables Potassium-Ion Chemistries, *Angew. Chem., Int. Ed.*, 2025, e202503904.
9 D. Gao, *et al.*, A survey of hybrid energy devices based on supercapacitors, *Green Energy Environ.*, 2023, **8**(4), 972–988.
10 S. Zi, *et al.*, Fe HS vacancies in a Prussian white cathode leads to enhanced Fe LS activity and electrode kinetics for boosted K+ storage, *J. Mater. Chem. A*, 2024, **12**(17), 10403–10411.
11 T. Ma, H. Yang and L. Lu, Development of hybrid battery–supercapacitor energy storage for remote area renewable energy systems, *Appl. Energy*, 2015, **153**, 56–62.
12 R. Powade and Y. Bhateshvar, Design of semi-actively controlled battery-supercapacitor hybrid energy storage system, *Mater. Today: Proc.*, 2023, **72**, 1503–1509.
13 Z. Dong, *et al.*, A survey of battery–supercapacitor hybrid energy storage systems: Concept, topology, control and application, *Symmetry*, 2022, **14**(6), 1085.
14 P. Forouzandeh, V. Kumaravel and S. C. Pillai, Electrode materials for supercapacitors: a review of recent advances, *Catalysts*, 2020, **10**(9), 969.
15 I. Dědek, *et al.*, Metal-organic framework/conductive polymer hybrid materials for supercapacitors, *Appl. Mater. Today*, 2022, **26**, 101387.
16 G. A. Snook, P. Kao and A. S. Best, Conducting-polymer-based supercapacitor devices and electrodes, *J. Power Sources*, 2011, **196**(1), 1–12.
17 X. Chen, R. Paul and L. Dai, Carbon-based supercapacitors for efficient energy storage, *Natl. Sci. Rev.*, 2017, **4**(3), 453–489.
18 J. Liu, *et al.*, High-performance flexible asymmetric supercapacitors based on a new graphene foam/carbon nanotube hybrid film, *Energy Environ. Sci.*, 2014, **7**(11), 3709–3719.
19 B. Khademi, *et al.*, High voltage binder free hybrid supercapacitor based on reduced graphene oxide/graphene oxide electrodes and "water in salt" electrolyte, *J. Energy Storage*, 2021, **43**, 103164.
20 P. Zheng, *et al.*, Multi boron-doping effects in hard carbon toward enhanced sodium ion storage, *J. Energy Chem.*, 2025, **100**, 730–738.
21 Y Zeng, *et al.*, A Fast and High Endurance Phase Change Memory Based on In-Doped Sb_2Te_3, *ACS Appl. Nano Mater.*, 2024, **7**(12), 13983–13990.
22 G. M. Tomboc, *et al.*, Hybrid layered double hydroxides as multifunctional nanomaterials for overall water splitting and supercapacitor applications, *J. Mater. Chem. A*, 2021, **9**(8), 4528–4557.
23 E. Bao, *et al.*, Porous MgCo2O4 nanoflakes serve as electrode materials for hybrid supercapacitors with excellent performance, *J. Colloid Interface Sci.*, 2022, **625**, 925–935.
24 T. Munawar, *et al.*, Superior electrochemical performance of neodymium oxide-based Nd2CeMO3 (M= Er, Sm, V) nanostructures for supercapacitor application, *J. Electroanal. Chem.*, 2022, **920**, 116614.
25 S. Xie and J. Gou, Compounds, Facile synthesis of Ni2P/Ni12P5 composite as long-life electrode material for hybrid supercapacitor, *J. Alloys Compd.*, 2017, **713**, 10–17.
26 S. S. Pujari, *et al.*, Hydrothermally synthesized nickel copper phosphate thin film cathodes for high-performance hybrid supercapacitor devices, *J. Energy Storage*, 2022, **52**, 105037.
27 S. Ghosh, *et al.*, Influence of transition metals (Cu and Co) on the carbon-coated nickel sulfide used as positive electrode material in hybrid supercapacitor device, *J. Compos. Sci.*, 2021, **5**(7), 180.
28 J. Rehman, *et al.*, Engineering of transition metal sulfide nanostructures as efficient electrodes for high-performance supercapacitors, *ACS Appl. Energy Mater.*, 2022, **5**(6), 6481–6498.
29 J. R. Xavier, S. Vinodhini and S. S. Chandraraj, Synthesis and electrochemical characterization of CNTs-based multi metal sulphide nanocomposite for supercapacitor applications, *J. Cluster Sci.*, 2023, **34**(4), 1805–1817.
30 L. Gao, *et al.*, Engineering multiple heterogeneous Co/CoSe/MoSe2 embedded in carbon nanofibers with Co/Mo–Se–C bonding towards high performance sodium ion capacitors, *Vacuum*, 2024, **228**, 113519.
31 P. A. Shinde, *et al.*, All Transition Metal Selenide Composed High-Energy Solid-State Hybrid Supercapacitor, *Small*, 2022, **18**(20), 2200248.
32 S. M. Bekhit, *et al.*, Electrodeposition of nickel selenides thin films for high-performance hybrid supercapacitor, *J. Energy Storage*, 2024, **83**, 110744.
33 Y. Jiao, *et al.*, Mixed-metallic MOF based electrode materials for high performance hybrid supercapacitors, *J. Mater. Chem. A*, 2017, **5**(3), 1094–1102.
34 C. Li, *et al.*, 3D Cu-BTC anchored on 2D MXene nanosheets using surface control approach for urea adsorption to achieve the regeneration of dialysate, *Sep. Purif. Technol.*, 2025, **373**, 133594.
35 M. Radhika, *et al.*, Electrochemical studies on Ni, Co & Ni/Co-MOFs for high-performance hybrid supercapacitors, *Mater. Res. Express*, 2020, **7**(5), 054003.
36 D.-G. Wang, *et al.*, Metal-organic framework-based materials for hybrid supercapacitor application, *Coord. Chem. Rev.*, 2020, **404**, 213093.
37 S. Sun, *et al.*, Controllable hydrothermal synthesis of Ni/Co MOF as hybrid advanced electrode materials for supercapacitor, *J. Electrochem. Soc.*, 2019, **166**(10), A1799.
38 L. Niu, *et al.*, Conductive metal–organic frameworks for supercapacitors, *Adv. Mater.*, 2022, **34**(52), 2200999.

39 T. Wang, *et al.*, Approaches to enhancing electrical conductivity of pristine metal–organic frameworks for supercapacitor applications, *Small*, 2022, **18**(32), 2203307.
40 S. Yu, *et al.*, Adjusting the electron configuration of MOFs-derived Ag/MnO1.1@C via electron transfer strategy to achieve a high-performance catalyst for potassium-oxygen batteries, *Appl. Surf. Sci.*, 2025, **709**, 163863.
41 Q. Guo, *et al.*, Alkali and alkaline earth metals in liquid salts for supercapatteries, *RSC Sustainability*, 2024, **2**(1), 101–124.
42 W. W. Lestari, *et al.*, Green and facile synthesis of MOF and nano MOF containing zinc (II) and benzen 1, 3, 5-tri carboxylate and its study in ibuprofen slow-release, *Mater. Chem. Phys.*, 2018, **204**, 141–146.
43 S. Zheng, *et al.*, Dual-ligand and hard-soft-acid-base strategies to optimize metal-organic framework nanocrystals for stable electrochemical cycling performance, *Natl. Sci. Rev.*, 2022, **9**(7), nwab197.
44 M. Z. Iqbal, *et al.*, Superior electrochemical performance of metal ligand framework-neodymium oxide composite for energy storage devices, *J. Electroanal. Chem.*, 2024, **963**, 118305.
45 C. Liu, *et al.*, In situ growth of three-dimensional MXene/metal–organic framework composites for high-performance supercapacitors, *Angew. Chem., Int. Ed.*, 2022, **61**(11), e202116282.
46 X.-y. Bu, *et al.*, 1T-VS2@ V2O3 synergistic nanoarchitecture-based lamellar clusters as the high conductivity cathodes of thermal batteries, *ACS Appl. Mater. Interfaces*, 2024, **16**(6), 7200–7210.
47 M. Z. Iqbal, *et al.*, Redox active pyridine-3, 5-di-carboxylate- and 1, 2, 3, 4-cyclopentane tetra-carboxylate-based cobalt metal–organic frameworks for hybrid supercapacitors, *RSC Adv.*, 2023, **13**(33), 22936–22944.
48 F. Sajid, *et al.*, Fabrication and analysis of barium-based metal organic framework characteristic properties, *Int. J. Mod. Phys. B*, 2022, **36**(28), 2250198.
49 D. Rattanaphra, *et al.*, Characterization of rare earths obtained from monazite concentrate processing and their application in esterification for biodiesel production, *Energy Rep.*, 2022, **8**, 6914–6928.
50 M. S. Khan, *et al.*, Unveiling the electrochemical advantages of a scalable and novel aniline-derived polybenzoxazole-reduced graphene oxide composite decorated with manganese oxide nanoparticles for supercapacitor applications, *J. Energy Storage*, 2023, **73**, 109109.
51 Y. Gogotsi and R. M. Penner, *Energy Storage in Nanomaterials–Capacitive, Pseudocapacitive, or Battery-like?*, ACS Publications, 2018, pp. 2081–2083.
52 P. Wang, *et al.*, Porous carbon for high-energy density symmetrical supercapacitor and lithium-ion hybrid electrochemical capacitors, *Chem. Eng. J.*, 2019, **375**, 122020.
53 P. Wen, *et al.*, Design and synthesis of Ni-MOF/CNT composites and rGO/carbon nitride composites for an asymmetric supercapacitor with high energy and power density, *J. Mater. Chem. A*, 2015, **3**(26), 13874–13883.
54 J. Sahu, *et al.*, Electrochemical and electronic structure properties of high-performance supercapacitor based on Nd-doped ZnO nanoparticles, *J. Energy Storage*, 2023, **59**, 106499.
55 M. Karuppaiah, *et al.*, Elevated energy density and cycle stability of α-Mn2O3 3D-microspheres with addition of neodymium dopant for pouch-type hybrid supercapacitors, *Electrochim. Acta*, 2020, **362**, 137169.
56 A. Qayyum, *et al.*, Performance optimization of Nd-doped LaNiO3 as an electrode material in supercapacitors, *Solid State Ionics*, 2023, **395**, 116227.
57 S.-W. Zhang, *et al.*, A high energy density aqueous hybrid supercapacitor with widened potential window through multi approaches, *Nano Energy*, 2019, **59**, 41–49.
58 C. Koventhan, *et al.*, Novel design of perovskite-structured neodymium cobalt oxide nanoparticle-embedded graphene oxide nanocomposites as efficient active materials of energy storage devices, *ACS Appl. Mater. Interfaces*, 2023, **15**(38), 44876–44886.
59 A. M. Afzal, *et al.*, Exploring the charge storage mechanism in high-performance Co@ MnO2-based hybrid supercapacitors using Randles–Ševčík and Dunn's models, *J. Appl. Electrochem.*, 2024, **54**(1), 65–76.
60 S. Pervez and M. Z. Iqbal, Capacitive and Diffusive Contributions in Supercapacitors and Batteries: A Critique of b-Value and the ν–ν1/2 Model, *Small*, 2023, **19**(48), 2305059.